

## Evolution of the electronic structure of a Mott system across its phase diagram: X-ray absorption spectroscopy study of $(V_{1-x}Cr_x)_2O_3$

F. Rodolakis,<sup>1,2,\*</sup> J.-P. Rueff,<sup>2,3</sup> M. Sikora,<sup>4,5</sup> I. Alliot,<sup>4,6</sup> J.-P. Itié,<sup>2</sup> F. Baudalet,<sup>2</sup> S. Ravy,<sup>2</sup> P. Wzietek,<sup>1</sup> P. Hansmann,<sup>7</sup> A. Toschi,<sup>7</sup> M. W. Haverkort,<sup>8</sup> G. Sangiovanni,<sup>7</sup> K. Held,<sup>7</sup> P. Metcalf,<sup>9</sup> and M. Marsi<sup>1</sup>

<sup>1</sup>Laboratoire de Physique des Solides, CNRS-UMR 8502, Université Paris-Sud, FR-91405 Orsay, France

<sup>2</sup>Synchrotron SOLEIL, L'Orme des Merisiers, Saint-Aubin, BP 48, FR-91192 Gif-sur-Yvette Cedex, France

<sup>3</sup>Laboratoire de Chimie Physique–Matière et Rayonnement, CNRS-UMR 7614, Université Pierre et Marie Curie, FR-75005 Paris, France

<sup>4</sup>ESRF, 6 rue Jules Horowitz, BP 220, FR-38043 Grenoble Cedex, France

<sup>5</sup>AGH University of Science and Technology, Krakow, Poland

<sup>6</sup>CEA/DSM/INAC/NRS 17 avenue des Martyrs, FR-38000 Grenoble, France

<sup>7</sup>Institut for Solid State Physics, Vienna University of Technology, AT-1040 Vienna, Austria

<sup>8</sup>Max-Planck-Institut für Festkörperforschung, Heisenbergstrasse 1, DE-70569 Stuttgart, Germany

<sup>9</sup>Department of Chemistry, Purdue University, West Lafayette, Indiana 47907, USA

(Received 2 September 2011; revised manuscript received 30 November 2011; published 13 December 2011)

$V_2O_3$  is an archetypal system for the study of correlation-induced, Mott-Hubbard metal-insulator transitions. Despite decades of extensive investigations, the accurate description of its electronic properties remains an open problem in the physics of strongly correlated materials, also because of the lack of detailed experimental data on its electronic structure over the whole phase diagram. We present here a high-resolution x-ray absorption spectroscopy study at the V  $K$  edge of  $(V_{1-x}Cr_x)_2O_3$  to probe its electronic structure as a function of temperature, doping, and pressure, providing an accurate picture of the electronic changes over the whole phase diagram. We also discuss the relevance of the parallel evolution of the lattice parameters, determined with x-ray diffraction. This allows us to draw two conclusions of general interest: First, the transition under pressure presents peculiar properties, related to a more continuous evolution of the lattice and electronic structure; second, the lattice mismatch is a good parameter describing the strength of the first-order transition, and is consequently related to the tendency of the system toward the coexistence of different phases. Our results show that the evolution of the electronic structure while approaching a phase transition, and not only while crossing it, is also a key element to unveil the underlying physical mechanisms of Mott materials.

DOI: [10.1103/PhysRevB.84.245113](https://doi.org/10.1103/PhysRevB.84.245113)

PACS number(s): 78.70.En, 71.20.Eh, 71.27.+a

### I. INTRODUCTION

A full understanding of electronic phase transitions in transition-metal oxides still poses many challenges in modern condensed matter physics. In fact, the relevant electronic correlations of partially filled  $3d/4d$  orbitals often drive these systems into situations where several energy scales are competing, so that their low-energy physics results are dramatically affected by very slight changes of the external control parameters such as temperature, pressure, doping, etc. In this class of materials, chromium-doped vanadium sesquioxide  $(V_{1-x}Cr_x)_2O_3$  has attracted considerable interest for undergoing a well-known first-order correlation-driven metal-insulator transition (MIT) between a paramagnetic insulating (PI) and a paramagnetic metallic (PM) phase.<sup>1</sup>

The phase diagram of  $(V_{1-x}Cr_x)_2O_3$  based on conductivity measurements<sup>2</sup> is shown in Fig. 1. At room conditions,  $V_2O_3$  is a paramagnetic metal (PM) with a corundum crystal structure. When the temperature is cooled down below the Néel temperature, it undergoes a structural and electronic transition toward a monoclinic, antiferromagnetic insulating phase (AFI), while doping with Cr at room temperature changes it to a paramagnetic insulator (PI), maintaining the original corundum structure. The application of an external pressure has the opposite effect, driving the PI Cr-doped  $V_2O_3$  back into the PM phase. For a small amount of chromium doping ( $0.9\% < x < 1.5\%$ ), the metallic phase can be reached by slightly decreasing the temperature. Thus, the

isostructural PM-PI transition can be induced by changing either temperature, doping, or pressure. This transition results in a jump in resistivity of several orders of magnitude<sup>3,4</sup> and is accompanied by an anisotropic discontinuity of the lattice parameters.<sup>1</sup>

In the corundum structure, each vanadium atom is surrounded by an octahedron of oxygen atoms, leading to a crystal-field splitting of the fivefold-degenerate  $d$  band into  $t_{2g}$  and  $e_g$  bands. Due to the trigonal distortion of the metallic site, the  $t_{2g}$  orbitals further split into  $e_g^\pi$  and  $a_{1g}$  bands, as illustrated in Fig. 2(a). It is nowadays widely accepted that the V  $3d^2$  ion has a  $S = 1$  spin state in all the phases, with a mixed  $(e_g^\pi, a_{1g})$  and  $(e_g^\pi, e_g^\pi)$  orbital occupation.<sup>5,6</sup> A combination of V  $L_{2,3}$  polarized x-ray absorption measurements and multiplet calculations revealed a large redistribution in the orbital occupation at the transition, with a ratio  $(e_g^\pi, a_{1g} : e_g^\pi, e_g^\pi) \approx 1 : 1$  and  $3 : 2$  in the PM and PI phases, respectively.<sup>7</sup> Taking the multiorbital nature of the MIT into account, recent theoretical models based on LDA + DMFT calculations succeeded in reproducing the main experimental features of the doping-induced PM-PI transition.<sup>8,9</sup> The differences between the densities of electron-addition spectra of the two phases are presented in Fig. 2(b) for the temperature-induced PM-PI transition at an  $x = 0.011$  doping level; detailed LDA + DMFT calculations of the momentum-integrated spectral functions for  $x = 0$  (PM) and  $x = 0.028$  (PI) can be found in Ref. 9.

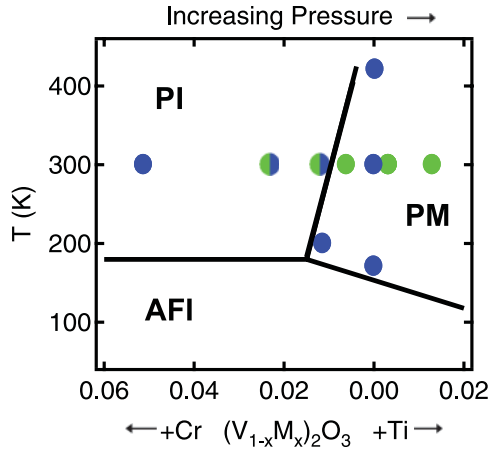


FIG. 1. (Color online) Phase diagram of  $(V_{1-x}Cr_x)_2O_3$  as a function of temperature, doping, and pressure according to Ref. 2, in which a pressure-doping equivalence has been empirically established to  $\pm 4$  kbar per percent of substituted atom. The blue (dark gray) dots indicate measurements at different temperatures and/or doping levels (at ambient pressure), while green (light gray) dots correspond to the 2.8% doping level at different pressures.

Experimentally, one of the most challenging issues is to analyze on equal footing the strong changes occurring in the different regions of the phase diagram of this compound under the effect of different external parameters. In order to help clarify this important issue, we present a high-resolution x-ray absorption spectroscopy (XAS) study at the V  $K$  edge of  $(V_{1-x}Cr_x)_2O_3$  in the two paramagnetic phases (PI and PM) for various doping levels ( $x = 0, 0.011, 0.028, 0.056$ ) measured at different temperatures [indicated by blue (dark gray) dots in Fig. 1] and pressure [green (light gray) dots]. In the framework of our previous theoretical understanding of V  $K$ -pre-edge XAS spectra,<sup>10</sup> we explore the changes in the electronic structure across the phase transition and its variations with external parameters (temperature, doping, and pressure) within each phase. To complete the description of the phase diagram, x-ray diffraction (XRD) experiments under pressure and temperature also have been carried out.

The paper is organized as follows: In Sec. II, the experimental details of the XAS measurements are described. General features of the XAS spectra through the MIT are discussed in Sec. III. Spectral changes as a function of temperature ( $T$ ), doping ( $x$ ), and pressure ( $P$ ), within a given phase, are presented and compared in Sec. IV. A discussion is finally provided in Sec. V.

## II. EXPERIMENT

The experiments were performed on the inelastic x-ray scattering (IXS) beamlines ID26 and BM30 at the European Synchrotron Radiation Facility (ESRF). The x-ray energies were selected by a cryogenically cooled double-crystal monochromator equipped with Si(311) [Si(220)] crystals at ID26 (BM30), which provided an energy bandwidth of 160 meV (280 meV) at the V  $K$  edge. XRD measurements as a function of temperature and pressure have been performed on the CRISTAL beamline at SOLEIL.

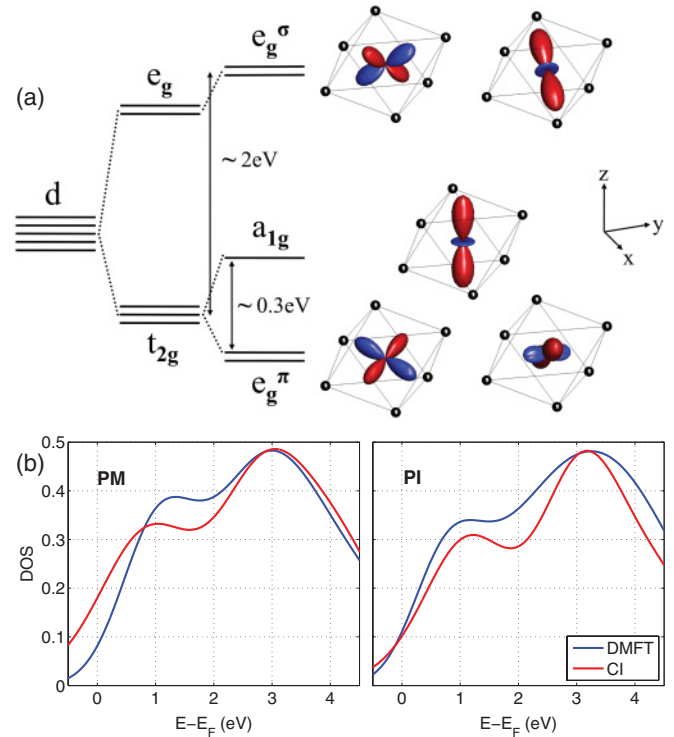


FIG. 2. (Color online) (a) Schematic representation of the  $d$  energy levels with the corresponding orbitals in the corundum structure. Due to the trigonal crystal field, the fivefold-degenerate  $d$  band splits into three bands:  $e_g^\sigma$ ,  $a_{1g}$ , and  $e_g^\pi$ . Numerical values are obtained from LDA calculation in Ref. 8. Computation of the incoherent spectra at the PI-PM transition: using dynamical mean-field theory (DMFT) and configuration interaction (CI) schemes (from Ref. 10).

To obtain an improved intrinsic resolution, the XAS spectra were acquired in the so-called partial fluorescence yield (PFY) mode.<sup>11</sup> The method is now widely established as a way to provide high-resolution absorption spectra, partly free from core-hole lifetime broadening effects.<sup>12</sup> The gain is particularly appreciable at the  $K$  pre-edge of transition metals as the  $1s$  core hole is extremely short lived with respect to the  $2p$  core hole, and the dipolar tail is strongly reduced. For this study, the PFY-XAS spectra were obtained by monitoring the intensity of the V- $K\alpha$  ( $2p \rightarrow 1s$ ) emission line as the incident energy is swept across the absorption edge. The V- $K\alpha$  line was measured with the help of an IXS Rowland-circle spectrometer equipped with a Ge(331) spherically bent analyzer with a bending radius of 860 cm. The same analyzer was used for all the PFY-XAS measurements.

We used powder specimens prepared from high-quality  $(V_{1-x}Cr_x)_2O_3$  single crystals from Purdue University, with various doping levels in the PM ( $x = 0$ ) and PI phases ( $x = 0.011, 0.028, 0.056$ ). The powder samples were compressed into pellets, well adapted to the fluorescence yield detection, occasionally with addition of boron nitride (BN) to reduce their density. A closed-cycle cryocooler was installed on the IXS spectrometer to control the temperature. When applying an external pressure, the PFY mode turned out to be difficult to implement because of the weak fluorescence signal through the pressure cell, and we consequently opted for standard

XAS measurements in transmission mode. To maximize the throughput, the powders ( $x = 0.028$ ) were loaded in a diamond anvil cell equipped with composite anvils made of a perforated diamond capped with a 500- $\mu\text{m}$  thin diamond anvil; we used a low-resolution Si(111) monochromator [instead of Si(311)] to improve the signal level. Pressure was measured *in situ* by standard ruby fluorescence techniques. We used silicon oil as a pressure-transmitting medium in the cell. It should be noted that the fact that both  $K$ -edge XAS and XRD are based on the use of hard x-rays (and hence compatible with diamond pressure cells), which was essential in terms of varying not only temperature and doping, but also pressure during our measurements.

We would like to point out that the PFY spectrum is nothing else but a specific cut through the general resonant inelastic x-ray scattering (RIXS) surface, where the spectral intensity is measured in resonant conditions as a function of both emitted and incident energies.<sup>13,14</sup> Figure 3 shows a typical RIXS measurement in  $(\text{V}_{0.989}\text{Cr}_{0.011})_2\text{O}_3$  measured at ID26. The incident energy is here limited to the pre-edge region, while the emitted energy is monitored in the vicinity of the  $K\alpha_1$  emission line. The left panel displays the XAS spectra retrieved from the RIXS intensity in both partial (PFY) and total (TFY) fluorescence yield mode. The latter was obtained by integrating the RIXS intensity over the entire emitted energy range, while the former is a cut over a 0.5-eV window around the  $K\alpha_1$  emission line (white dash on the right panel). The sharpening effect is evident in the PFY acquisition mode. No missing spectral weight is observed in the PFY spectrum of  $(\text{V}_{0.989}\text{Cr}_{0.011})_2\text{O}_3$ , which is found to be almost identical, except for the enhanced resolution effects, to the standard x-ray absorption. On the other hand, the choice of the PFY emission energy affects the positions of the lowest-energy peak structure, as its maximum intensity in the RIXS surface is located slightly out of the  $K\alpha_1$  emission line. Such artificial shift of 0.2 eV of the low-energy peak has been taken into

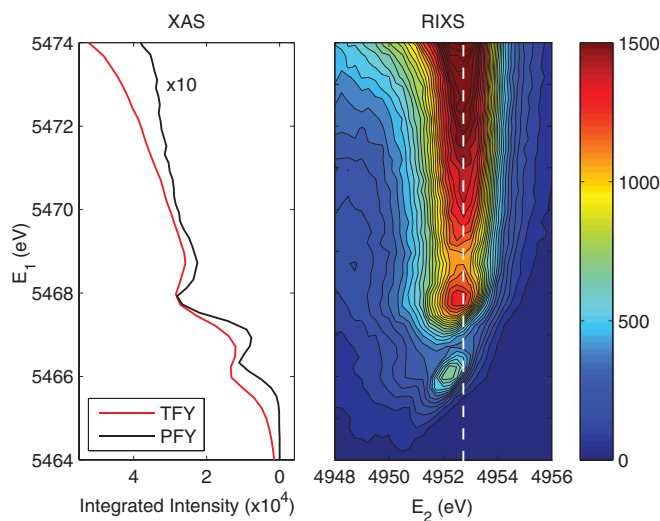


FIG. 3. (Color online) (a)  $V K$ -pre-edge x-ray absorption spectra in a  $(\text{V}_{0.989}\text{Cr}_{0.011})_2\text{O}_3$  single crystal measured at room conditions in the partial (PFY) and total (TFY) fluorescence modes. (b) RIXS surface as a function of incident ( $E_1$ ) and emitted ( $E_2$ ) photon energy in the vicinity of the pre-edge region.

account in the analysis, and it therefore has no impact on the final results of our study. Notice that the asymmetry of the RIXS feature in the pre-edge region may be due to nonlocal dipolar transitions.<sup>15</sup> This will be further discussed in the following section.

### III. SPECTRAL FEATURES OF THE $V K$ EDGE

Figure 4 shows the isotropic  $V K$ -edge PFY absorption spectra through the  $T$ -induced MIT. The full spectra are displayed in Fig. 4(a) for both the PM (200 K) and PI (300 K) phase in an  $x = 0.011$  powder sample. The spectra were normalized at the inflection point of the first extended x-ray absorption fine structure (EXAFS) oscillations. They can be decomposed in two spectral regions: the former is the main edge [above the onset (D) at 5475 eV], corresponding to  $1s \rightarrow 4p$  dipolar transitions; the latter is the pre-edge (at lower energy), mainly corresponding to  $1s \rightarrow 3d$  quadrupolar transitions, shown in Fig. 4(b) on an expanded energy scale. Visible spectral changes are observed through the transition, as it is clearly shown by the spectral difference (PM-PI). The integrated intensity of the difference curve averages to zero

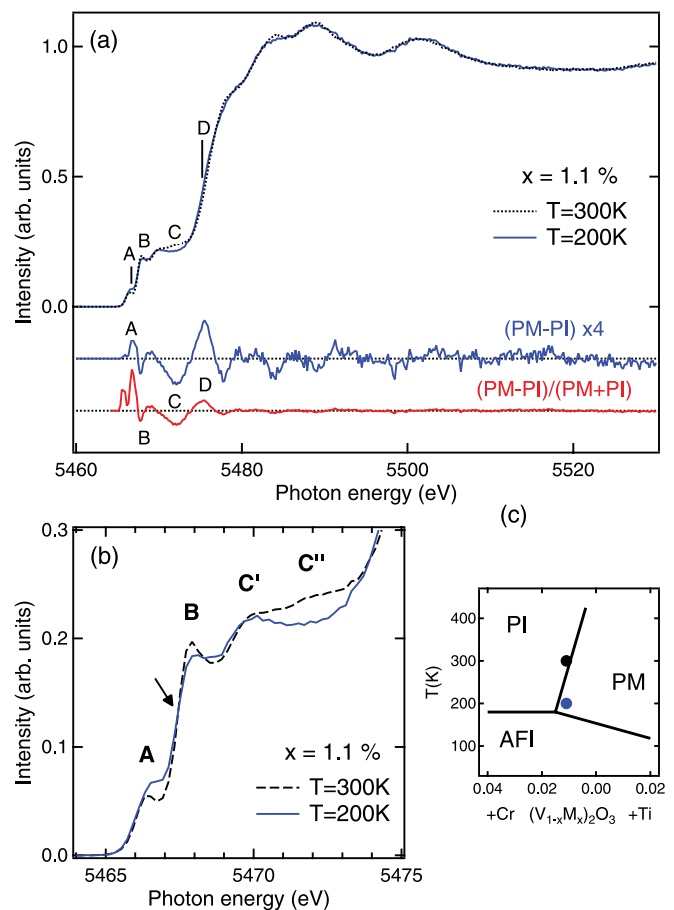


FIG. 4. (Color online) (a)  $V K$ -edge x-ray absorption spectra in a  $(\text{V}_{0.989}\text{Cr}_{0.011})_2\text{O}_3$  powder sample measured as a function of temperature in the PI (300 K, dashed line) and PM (200 K, solid line) phases in PFY mode; below, the blue (dark grey) curve shows the absolute spectral difference, while the red (light grey) curve represents the relative spectral difference; (b) pre-edge region; (c) corresponding points in the phase diagram.

over the whole spectra, but also in the pre-edge region (from 5460 to 5475 eV), suggesting a conservation of the spectral weight (SW) through the transition within the pre-edge. A visual inspection of the relative spectral differences shows that these changes occur principally in the pre-edge region (peaks A, B, and area C) and at higher energies at the rising edge (D); beyond the main edge, the spectra are almost indistinguishable. As both paramagnetic phases have the same crystallographic structure, we can conclude that these differences are only due to modifications in the electronic structure occurring at the MIT under the effect of electronic correlations.

In this work, we more specifically focus on the pre-edge region, and on how it evolves through the MIT as a function of the various external parameters. The pre-edge regions for both paramagnetic phases present well-defined spectral features, labeled (A, B, C), which vary in intensity and shape as the system is driven through the MIT. The broad feature C can be further split into two substructures at about 5470 eV ( $C'$ ) and 5472 eV ( $C''$ ), the latter exhibiting the largest change with an inversion of curvature at the transition.

Understanding the spectral features of the whole pre-edge region in  $(V_{1-x}Cr_x)_2O_3$  remains a complex task. First, the V sites lack inversion symmetry along the  $c$  axis, resulting in a slight onsite mixing of  $3d$  and  $4p$  vanadium states. As a consequence, dipole transitions to the formerly “pure”  $3d$  states are possible to a certain extent (note that such mixing leads to interference effects that can be visible in elastic scattering experiments<sup>16</sup>). Second, the ground states of the PM and the PI phases are strongly multiorbital in nature as it involves a mixing of the  $e_g^\pi$  and  $a_{1g}$  orbitals. The PI-PM transition is characterized by a change in the occupancy ratio between the  $(e_g^\pi, a_{1g})$  and  $(e_g^\pi, e_g^\pi)$  states, which is markedly smaller in the PI with respect to the PM phase.<sup>7,8</sup> The detailed analysis of the lowest-energy pre-edge features of the V  $K$  edge of  $(V_{1-x}Cr_x)_2O_3$  has been the object of our previous paper.<sup>10</sup>

Starting from the higher-energy region of the pre-edge, it may be tempting to associate peak C to nonlocal  $1s \rightarrow 3d$  dipole excitations to a neighboring V atom.<sup>17</sup> The cross section for such a transition would strongly depend on the overlap integrals of the vanadium and oxygen orbitals, i.e., the  $4p$ - $O$ - $3d$  intersite hybridization. This nonlocal hybridization, in turn, is expected to sensitively depend on the atomic distances:<sup>18</sup> the smaller the distances among the atoms, the larger the overlap integrals. Keeping this argument in mind, we can revisit the lattice parameters for the PM and PI phases, respectively. Namely, although the MIT in the paramagnetic phase is isostructural, we find a discontinuity in the evolution of the lattice parameters at the transition. In particular, the basal  $a$  axis decreases,<sup>1</sup> resulting in a reduced  $V$ - $O$  bond, which would influence the above-mentioned nonlocal excitations. And, indeed, we see in the experimental data the changes of the lattice parameters reflected in a strong change of the  $C''$  intensity, which we will further investigate in Sec. IV B. However, the idea that smaller lattice parameters lead directly to an increase of spectral weight is not confirmed by our measurements and is probably too naive. While experimental evidence suggests to include also nonlocal excitations in a comprehensive description of the entire absorption edge,

the theoretical realization is far from being trivial: the most important states for nonlocal excitations are the vanadium  $e_g$  states, which hybridize more strongly (forming  $\sigma$  bonds) with ligand orbitals. In that way, they can be seen as the link between the localized and the itinerant part of the spectrum, rendering a proper treatment extremely difficult since no approach that relies on taking either of these limits will be completely satisfactory.

The interpretation of peaks A and B, which correspond to excitonic features involving the  $t_{2g}$  states, is instead much clearer and certainly more informative about the the low-energy physics of the MIT in  $V_2O_3$ . Specifically, with the help of multiplet calculations in the configuration interaction (CI) scheme, combined with LDA + DMFT calculations,<sup>10</sup> we confirmed the change in the  $(e_g^\pi, e_g^\pi):(e_g^\pi, a_{1g})$  occupancy ratio from 50 : 50 in the PM phase to 35 : 65 in PI phase, in good agreement with Ref. 7. The isotropic CI-based calculated XAS spectra agree well with the experimental data as for both the energy splitting of the features A and B and the ratio of their SW, which increases in the PM phase. As a result, peaks A and B in the pre-edge region have to be related to incoherent (local) excitations involving  $t_{2g}$  degrees of freedom.<sup>10</sup>

An important outcome from these calculations is that the intensity ratio of the first two pre-edge features (i.e., the ratio between peaks A and B) is a key spectral parameter related to the differences between PM and PI: the larger the ratio between the spectral weight of A and B, the larger the  $a_{1g}$  orbital occupation.

In our previous work,<sup>10</sup> we focused our interest on the differences among  $P$ -,  $T$ -, and  $x$ -induced transitions in  $(V_{1-x}Cr_x)_2O_3$ , but interesting insight can be also gained by analyzing differences in XAS spectra as a function of these external parameters within a given phase. In this paper, we explore in detail how the XAS spectroscopic features in pre-edge (A, B,  $C'$ , and  $C''$ ) evolve while moving across the phase diagram, and discuss how these changes are related to the physics of the system.

#### IV. XAS SPECTRA ACROSS THE PHASE DIAGRAM

In this section, we present high-resolution XAS measurements of  $(V_{1-x}Cr_x)_2O_3$  over an extensive portion of its phase diagram. The effects of each thermodynamic parameter (temperature, doping, pressure) will be discussed in the forthcoming individual sections. For sake of clarity, the main spectroscopic results will be then presented in a summary figure at the end of the paper (Fig. 9) to give a general picture of their evolution. In parallel, a summary figure for the lattice parameters will be also presented at the end (Fig. 11), where the physical implications of our results will be discussed. We found this very useful since the subtle interplay between electronic and lattice degrees of freedom plays a key role in the physics of  $(V_{1-x}Cr_x)_2O_3$ : in the effort of providing the reader with as much information as possible, we collected in Fig. 11 the results of x-ray diffraction measurements from previous authors<sup>1</sup> together with data of ours. We recall here the main trends of the structural behavior of  $(V_{1-x}Cr_x)_2O_3$ , which are summarized in Fig. 11 for the PI-PM transition as a function of temperature, doping, and pressure (left and middle panels). For all the thermodynamic parameters under consideration, at

the PI-PM transition, an increase can be observed for  $c$ , while  $a$  decreases, resulting in a jump of the  $c/a$  ratio. Data obtained by crossing the transition in temperature are remarkably identical to those measuring across the doping-induced transition from Ref. 1. On the other hand, measurements under pressure show the same trend, but with a smaller discontinuity.

These structural effects should be kept in mind during the analysis of the electronic properties, based on the XAS data presented hereafter.

### A. Spectral changes with temperature and doping

Figure 5(a) shows the spectra of  $(V_{1-x}Cr_x)_2O_3$  for various doping levels ( $x = 0, 0.011, 0.028, 0.056$ ) at ambient conditions. As shown in the phase diagram [Fig. 5(c)], the sample is stabilized in the PM phase for  $x = 0$  and in the PI phase for the other doping levels. To help visualize the spectral changes as a function of external parameters, we plotted in Fig. 5(b) the differences between the different data sets and the one for  $x = 0.011$ . We outlined in our previous paper<sup>10</sup> the remarkable similarity between temperature- and doping-induced changes through the MIT in the pre-edge XAS features: at low energy (A, B), the spectra measured through the doping-induced MIT are identical within the experimental uncertainty to those measured through the  $T$ -driven transition, with a comparable A/B intensity ratio variation of  $\approx 15\%$ .

Here, we can see that the difference spectra in Fig. 5(b) show barely any  $x$  dependence in the PI phase, which is consistent with the recent optical conductivity measurements performed by Lupi *et al.*<sup>19</sup> In the frame of our interpretation, this indicates that the orbital occupation is rather insensitive to the doping level within the PI phase, in good agreement with the results obtained by Park *et al.*<sup>7</sup> Consequently, local incoherent excitations probed by  $K$ - and  $L_{2,3}$ -edge XAS on powder samples do not seem to be directly affected by local distortions induced by chemical substitution,<sup>20</sup> even though an anomalous behavior has recently been observed in the  $C'$ ,

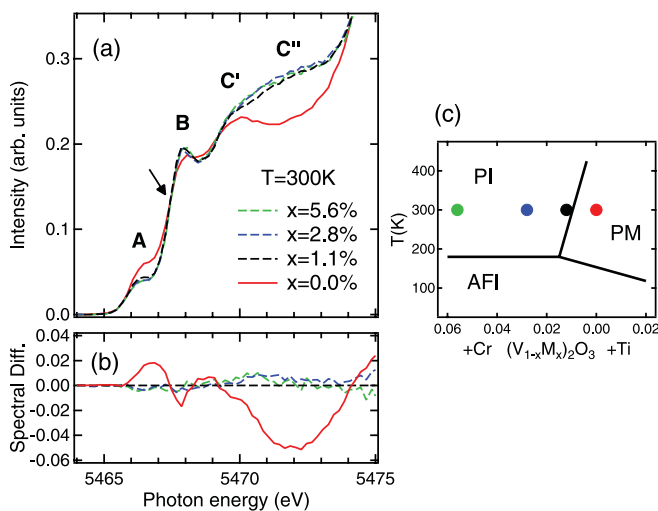


FIG. 5. (Color online) V  $K$ -pre-edge x-ray absorption spectra for a  $(V_{1-x}Cr_x)_2O_3$  powder sample at room conditions as a function of doping ( $x = 0, 0.011, 0.028, 0.056$ ) in PFY mode; (b) spectral differences, with respect to the  $x = 0.011$  spectra; (c) corresponding points in the phase diagram.

$C''$  spectral region for single crystals<sup>21</sup> in parts of the phase diagram where, as recently evidenced, the PI and PM phases coexist.<sup>19</sup>

From this analysis, it appears that both A/B and C change at the PI/PM transition, while both remain constant within the Mott insulating (PI) phase. Their behavior within the correlated metallic (PM) phase is instead not as trivial, suggesting that the direct dependence on electron correlations is more pronounced for A/B than for C.

Figure 6 displays the pre-edge region of XAS spectra in paramagnetic metallic  $V_2O_3$  as a function of temperature. Only negligible spectral changes are observed in the pre-edge structures between 300 and 170 K; at higher temperature, 420 K, more pronounced modifications are visible for the low-energy excitations (in particular, for A). Thus, while the intensity ratio  $I(A)/I(B)$  remains nearly constant when the sample is heated from 170 to 300 K, a drop of  $\approx 10\%$  is observed between 300 and 420 K, indicating a significant change in the orbital occupation. This change is comparable with the one measured across the  $(T,x)$ -MIT, as can be seen by comparing the evolution of the intensity ratio in Figs. 9(e) and 9(f). It could be related to the proximity of the crossover region, which results in a variation of the conductivity in pure  $V_2O_3$  as a function of temperature:<sup>4</sup> starting from low temperature, the resistivity shows a monotonic decrease, which is markedly enhanced while approaching the crossover region around 425 K.<sup>22</sup> This is accompanied by a slight change in the lattice parameters, reproduced in Fig. 11 (right panel), which show as well an anomaly near to the crossover region.<sup>1</sup> All together, these results indicate that at the edge of the crossover region at 420 K, differences between PI and PM already start to blur out.

A detailed XAS study at high temperature (above 420 K) on both sides of the transition line should certainly provide interesting information on the peculiar electronic properties in

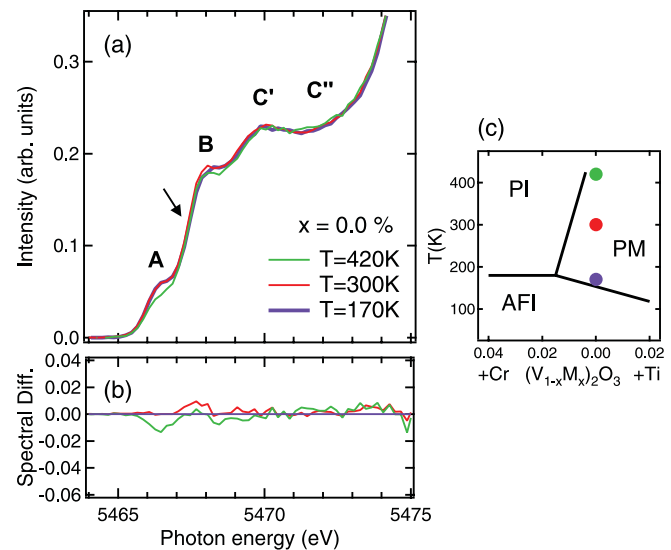


FIG. 6. (Color online) V  $K$ -pre-edge x-ray absorption spectra for a  $V_2O_3$  (PM) powder sample as a function of temperature in PFY mode ( $T = 170, 300$ , and  $420$  K); (b) spectral differences, with respect to the low-temperature spectra; (c) corresponding points in the phase diagram.

the crossover region, where a clear distinction between metal and insulator phases no longer exists:<sup>23</sup> In fact, as it can be seen in Fig. 11, the values of  $c/a$  in the CO region tend progressively to the range corresponding to the PI phase.

Overall, except for these effects occurring when entering the crossover, no significant changes are visible in the low-energy XAS spectral features when probing different  $(T, x)$  points in a given thermodynamic phase. By changing these external parameters, one would expect the coherent part of the electron density of states to be affected by the subtle effects linked to disorder. In fact, using bulk sensitive photoemission, it has been shown that the quasiparticle peak observed in the paramagnetic metallic phase presents a clear  $T$  dependence, while the lower Hubbard band remains almost unchanged.<sup>24</sup> This behavior is also observed as a function of doping level:<sup>25</sup> at room temperature, the coherent SW is strongly reduced as the doping level is increased, while the lower Hubbard band is virtually not affected. This confirms that even the low-energy spectral features in the XAS  $V K$ -pre-edge region are directly linked only to the incoherent part of the electron density of states.

Nevertheless, significant changes in the correlated metal XAS spectral yield appear in one part of the PM region of the phase diagram; as shown in Fig. 7, a marked difference is visible between the  $C''$  feature for  $x = 0.011$  at  $T = 200$  K, and  $x = 0$  at  $T = 300$  K. This difference can be linked to the bad-metallic behavior observed from resistivity<sup>4</sup> and optical conductivity<sup>19</sup> measurements in  $(V_{0.989}Cr_{0.011})_2O_3$ , differently from  $V_2O_3$ . As unambiguously demonstrated in Ref. 19, this bad-metallic behavior can be explained by the presence of phase separation, characterized by the presence of coexisting metallic and insulating domains. This coexistence was directly observed using a spectromicroscopic approach,<sup>26</sup> a method with a well-established capability of resolving metallic from insulating microscopic regions<sup>27</sup> and of observing differences in electronic band structures,<sup>28</sup> which could appear macroscopically homogeneous.<sup>29</sup> Subsequently, the effects of this phase separation on the XAS spectra of  $(V_{1-x}Cr_x)_2O_3$  single crystals were analyzed in detail,<sup>21</sup> showing an anomalous behavior of a feature corresponding to the spectral region that we indicate with  $C''$  and that has been related to the presence of highly distorted  $VO_6$  octahedra. In our case, where only powder samples are considered, we notice that the doped metallic spectrum ( $PM_{1.1\%}$ ) can be satisfactorily reproduced with a linear combination of the ( $PM_{0\%}$ ) and ( $PI_{1.1\%}$ ) spectra:

$$f * PM_{0\%} + (1 - f) * PI_{1.1\%}.$$

The best fit is obtained for  $f = 0.54$  (crosses in Fig. 7). This value is in good agreement with the volume fraction  $f = 0.42$  determined using a spatially resolved method such as scanning photoelectron microscopy<sup>30,31</sup> and successfully used for theoretical calculations of the spatially averaged optical conductivity<sup>19</sup> (the larger value obtained here for  $f$  can be explained considering the slightly lower temperature for the measurements presented here). We would also like to emphasize that these results have been consistently obtained with different sets of measurements performed on different synchrotron radiation beamlines, thanks also to a rigorous

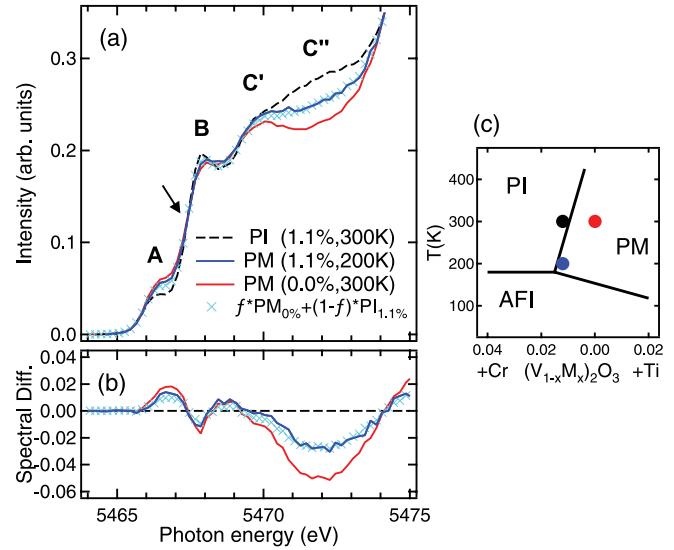


FIG. 7. (Color online)  $V K$ -pre-edge x-ray absorption spectra for a  $(V_{1-x}Cr_x)_2O_3$  powder sample as a function of temperature and doping level in PFY mode ( $x = 0, 0.011$  and  $T = 200$  and  $300$  K); crosses represent a linear combination of the room-temperature spectra ( $PM_{0\%}$  and  $PI_{1.1\%}$ ) for a value of  $f = 0.54$ ; (b) PI-PM spectral differences; (c) corresponding points in the phase diagram.

control of the experimental parameters (temperature, pressure, hysteresis at the phase transition, etc.).

### B. Spectral changes with pressure

Figure 8(a) displays the pressure-dependent pre-edge XAS spectra up to 15 kbar in a  $(V_{1-x}Cr_x)_2O_3$  ( $x = 0.028$ ) powder sample; the MIT happens between 5 and 7 kbar (cf. Fig. 11).

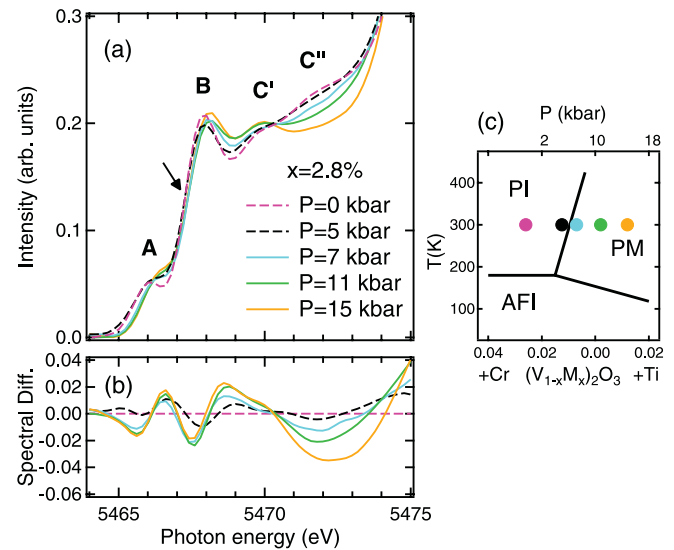


FIG. 8. (Color online)  $V K$ -pre-edge x-ray absorption spectra in a  $(V_{1-x}Cr_x)_2O_3$  ( $x = 0.028$ ) powder sample measured as a function of pressure in the PI ( $P \leq 5$  kbar, dashed lines) and PM ( $P \geq 7$  kbar, solid lines) phases; (b) spectral differences, with respect to the room-pressure spectra; the pressure scale in the phase diagram (c) refers to the  $x = 0.028$  doping.

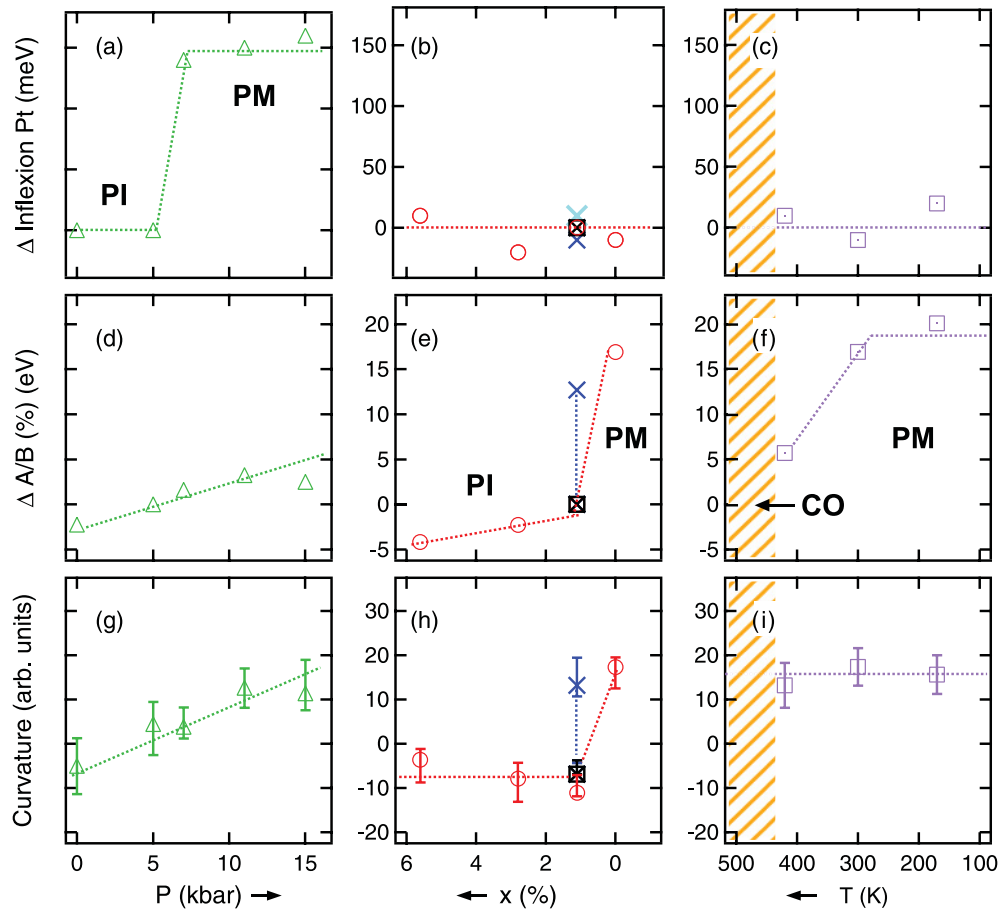


FIG. 9. (Color online) Pre-edge spectral feature evolution as a function of pressure ( $x = 2.8\%$ , green triangles; the pressure refers to the  $x = 2.8\%$  doping), doping level (red circles), and temperature ( $x = 0\%$ , purple square): (a)–(c) relative displacement of the inflection point between the first two peaks, indicated by the black arrow on the pre-edge spectra; (d)–(f) relative variation of the intensity ratio  $I(A)/I(B)$ ; (g)–(i) inverse radius of curvature at the  $C''$  point. Shaded areas indicate the crossover (CO) region. On the middle panel, we present the data obtained in the  $(V_{0.989}Cr_{0.011})_2O_3$  sample across the temperature-induced MIT in the PI (300 K, black crossed square) and PM phases (200 K, dark blue cross); the light blue cross [panel (b)] corresponds to the data obtained in TFY mode, showing these results are independent of the detection mode.

The spectra here obtained in transmission geometry have been deconvolved from the  $1s$  Lorentzian lifetime broadening (1 eV FWHM) using the *deconv* package from the GNAXS code<sup>32–34</sup> so as to match the improved resolution of the data sets measured by PFY-XAS.

All the spectral features (A, B,  $C'$ ,  $C''$ ) evolve under pressure in both paramagnetic phases PI ( $P \leq 5$  kbar) and PM ( $P \geq 7$  kbar). We observed a modification in the first two peaks intensity, but these effects are not comparable to the abrupt modification of the spectral lineshape observed at the  $T$  or doping-induced MIT: we measured the intensity ratio  $I(A)/I(B)$  to a raise of 15% by crossing the transition with temperature or doping versus only few percent with pressure ( $< 2\%$ ). The largest changes are observed in the  $C$  spectral region. While  $C'$  slowly increases with pressure,  $C''$  acquires a concave lineshape that progressively deepens with pressure as soon as the MIT is crossed. But, the two regimes can be better visualized by inspecting the position of the inflection point between A and B as a function of pressure [cf. Fig. 9(a)], which measures the rigid shift of the pre-edge with respect to the

main edge. The discontinuous jump at 5 kbar clearly denotes the PI-PM transition line, while only negligible changes are visible within the two phases.

Actually, the evolution of the  $P$ -dependent difference spectra [Fig. 8(b)] is rather continuous, and the  $P$ -induced MIT results in a rigid shift of the spectral weight of the first two peaks up in energy by  $\sim 0.15$  eV, as explained in our previous paper.<sup>10</sup> These results, resumed in Fig. 9, are in striking contrast with what is seen as a function of ( $T$ ,  $x$ ).

## V. DISCUSSION

To make the comparison between the different thermodynamic parameters easier, we have extracted the evolution of different spectral features. These results are summarized in Fig. 9, which shows (a)–(c) the relative displacement of the inflection point between the first two peaks (indicated by the black arrow on the pre-edge spectra figures); (d)–(f) the relative variation of the intensity ratio  $I(A)/I(B)$ , determined using the fitting procedure exposed in Fig. 10; (g)–(i) the inverse radius of curvature at the  $C''$  point.

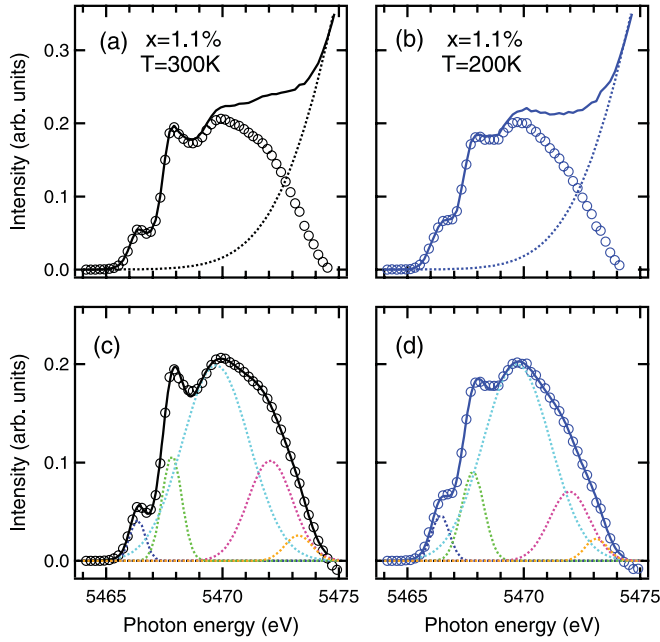


FIG. 10. (Color online) Illustration of the pre-edge fitting procedure for the data obtained on the  $(V_{0.989}Cr_{0.011})_2O_3$  sample across the temperature-induced MIT: after subtraction of the dipolar tails (dotted lines, top panels), the remaining features (circles) are fitted using five Gaussian functions (dotted lines, bottom panels). The maxima of the first two Gaussians corresponding to the peaks A and B are used to display the  $I(A)/I(B)$  evolution in Figs. 9(d)–9(f).

A comparative analysis of the effects of the various thermodynamic parameters leads to the following observations: (i) within a phase, the spectral features show barely any dependence as a function of temperature and doping level, in striking contrast with pressure; (ii) while  $(T, x)$ -induced transitions result in a discontinuous evolution of a specific spectral feature across the MIT, the pressure dependence of this spectral feature is virtually continuous, and vice versa. These results confirm the peculiar role of pressure in the phase diagram of  $(V_{1-x}Cr_x)_2O_3$ .

As the pressure is increased, the continuous lineshape modifications of the pre-edge features for both paramagnetic phases [cf. Figs. 9(d) and 9(g)] can be first attributed to the variation of the lattice parameter under compression: applying an external pressure induces a variation of lattice parameters within both PM and PI, and not mainly at the transition as observed as a function the doping level (left versus middle panel in Fig. 11). The resulting variation in the  $U/W$  ratio changes the correlation effects, which one can observe in the pre-edge features.

This interpretation is no longer evident considering the strong evolution of the lattice parameters as a function of temperature in the metallic phase. However, one should note that XAS is a very local probe, contrary to XRD. Understanding the exact interplay between electronic and lattice degrees of freedom would require a more local structural study, such as EXAFS.

In Fig. 9(d), the  $I(A)/I(B)$  ratio is displayed as a function of pressure. We observe a continuous increase of about 5% over the entire pressure range. The absence of any discontinuity

through the MIT suggests that this evolution is not related to the transition itself, as can be observed for temperature or doping, but rather to the pressure increase, regardless of the considered phase. In the frame of the arguments discussed above, this evidences a slight increase of the  $a_{1g}$  occupation in the ground state, while  $U/W$  decreases by increasing  $P$ . This result is in agreement with the theoretical evolution predicted by Keller *et al.*,<sup>8</sup> and supports our statement that different mechanisms apply for the pressure- and temperature- (or doping-) induced transitions.<sup>10</sup>

## VI. CONCLUSION

We performed a high-resolution x-ray absorption spectroscopy study at the V  $K$  edge of  $(V_{1-x}Cr_x)_2O_3$  to probe its electronic structure through the isostructural metal-insulator transition and across its phase diagram as a function of temperature, doping, and pressure.

In particular, our detailed analysis of the V  $K$ -pre-edge region over an extensive set of data confirms our previous interpretation of the nature of the various spectral features: in particular, the ratio between A and B provides a direct indication of the orbital occupation of the  $a_{1g}$  orbital, and is consequently directly related to electron correlation effects. For the interpretation of C', C'', further modeling efforts are necessary since their character in-between the itinerant and local limit has, so far, limited a profound theoretical description. It is, however, clear that the shape of this spectral region is extremely sensitive to the coexistence of the two phases,<sup>21</sup> although the origin of this sensitivity (structural, screening effects) is not fully understood.

By analyzing this spectroscopic information across the phase diagram, and by comparing it with novel and old XRD measurements, we were able to confirm with an extensive set of data the key role played by the interplay of electron correlations and slight structural changes in the physics of this model Mott-Hubbard system, since our hard x-ray-based techniques allowed us to compare the effects of doping, temperature, and pressure. This interplay gives support to some of the most recent theoretical models describing this system<sup>8,9</sup> and explains two important effects of general interest for the physics of the MIT of realistic multiband systems.

On one side, our comparative study among the different thermodynamic parameters confirms the singularity of pressure in the phase diagram of this prototype system. This is due to the fact that, compared to doping, the action of pressure accommodates the lattice mismatch between metal and insulator in a less discontinuous way: this translates into a smaller  $c/a$  jump at the transition, associated with an unchanged occupation but increased bandwidth of the  $a_{1g}$  orbitals. This less evident discontinuity at the transition is associated to more continuous and evident changes in parts of the phase diagram that are far away from the transition.

On the other side, it is also clear that the tendency of the system toward separation and coexistence of phases is also related at the amount of lattice mismatch it has to accommodate at the transition. By comparing our results for the PM phase in two points of the phase diagram, which are both close to the PM/PI phase transition, namely,  $x = 0.011$ ,  $T = 200$  K, and  $x = 0$ ,  $T = 420$  K, it is clear that the former presents

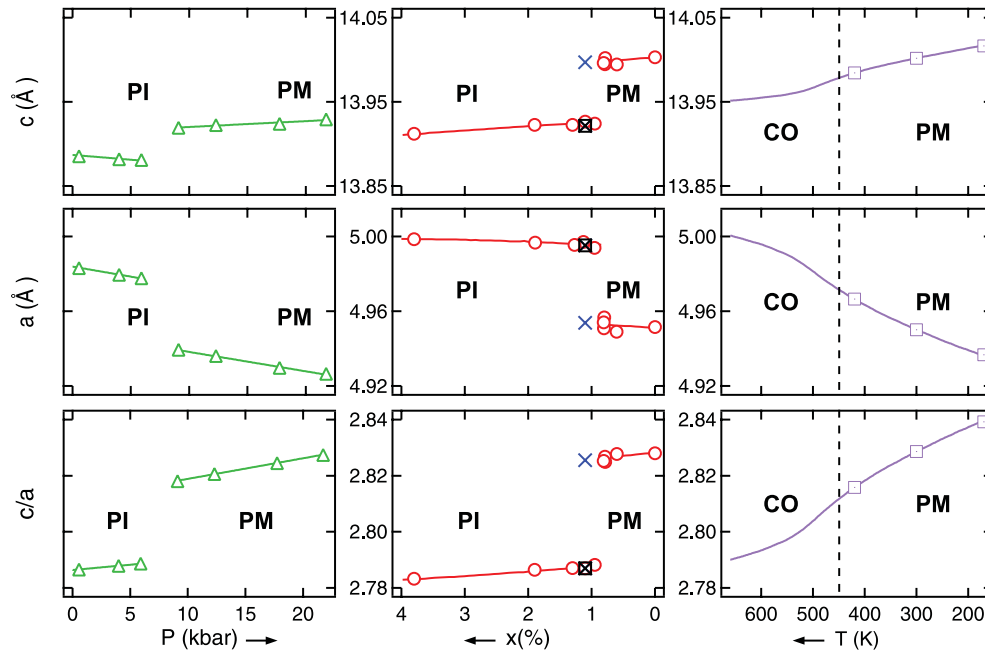


FIG. 11. (Color online) Lattice parameters as a function of pressure ( $x = 2.8\%$ , green triangles; the pressure scale refers to the  $x = 2.8\%$  doping), doping level (red circles, from Ref. 1), and temperature ( $x = 0\%$ , purple square, from Ref. 1). On the middle panel, we also present the lattice parameters measured in a  $(V_{0.989}Cr_{0.011})_2O_3$  sample across the temperature-induced MIT in the PI (300K, black crossed square) and PM phases (200K, blue cross).

stronger evidence for phase coexistence: since the system has to accommodate a  $c/a$  discontinuity of 0.04, in the proximity of the phase transition, it will tend to form domains with the PI and PM lattice parameters<sup>19</sup> to accommodate this difference. For  $x = 0$ ,  $T = 420$  K, we are instead very close to the critical point and the crossover region, and the structural differences between PM and PI are reduced, as it is evident from the corresponding  $c/a$  values: the fact that there is less lattice mismatch to accommodate explains why in this point, close to a Mott instability, there is no evidence of the dramatic phase separation found for  $x = 0.011$ ,  $T = 200$  K, even though the thermodynamic distance from the PM/PI phase transition is similar. Alternatively, and more fundamentally, we may regard the PI-PM mismatch as the strength of the “first-order” transition (where  $c/a$  can be regarded as the order parameter), and we may observe that this strength reflects the tendency toward phase separation: at low temperatures, i.e., for

$x = 0.011$ ,  $T = 200$  K, there is indeed such a strong tendency. In contrast, at  $x = 0$ ,  $T = 420$  K, which is close to the critical point at which the first-order transition line terminates, not only the lattice discontinuity gets very small, but we also do not find any strong tendency toward phase separation.

In conclusion, this work shows that it is important for strongly correlated materials to combine the study of structural and electronic properties, and that exploring the way the material evolves while approaching a phase transition, and not only while crossing it, is also a fundamental piece of information in the effort of understanding these systems.

#### ACKNOWLEDGMENT

We acknowledge partial financial support from the RTRA “Triangle de la Physique” and from a BQR of the Université Paris-Sud.

\*Current address: Material Science Division, Argonne National Laboratory, Argonne, Illinois 60439, USA.

<sup>1</sup>D. B. McWhan and J. P. Remeika, *Phys. Rev. B* **2**, 3734 (1970).

<sup>2</sup>D. B. McWhan, A. Menth, J. P. Remeika, W. F. Brinkman, and T. M. Rice, *Phys. Rev. B* **7**, 1920 (1973).

<sup>3</sup>D. B. McWhan, T. M. Rice, and J. P. Remeika, *Phys. Rev. Lett.* **23**, 1384 (1969).

<sup>4</sup>H. Kuwamoto, J. M. Honig, and J. Appel, *Phys. Rev. B* **22**, 2626 (1980).

<sup>5</sup>S. Y. Ezhov, V. I. Anisimov, D. I. Khomskii, and G. A. Sawatzky, *Phys. Rev. Lett.* **83**, 4136 (1999).

<sup>6</sup>L. Paolasini, C. Vettier, F. de Bergevin, F. Yakhov, D. Mannix, A. Stunault, W. Neubeck, M. Altarelli, M. Fabrizio, P. A. Metcalf, and J. M. Honig, *Phys. Rev. Lett.* **82**, 4719 (1999).

<sup>7</sup>J.-H. Park, L. H. Tjeng, A. Tanaka, J. W. Allen, C. T. Chen, P. Metcalf, J. M. Honig, F. M. F. de Groot, and G. A. Sawatzky, *Phys. Rev. B* **61**, 11506 (2000).

<sup>8</sup>G. Keller, K. Held, V. Eyert, D. Vollhardt, and V. I. Anisimov, *Phys. Rev. B* **70**, 205116 (2004).

- <sup>9</sup>A. I. Poteryaev, J. M. Tomczak, S. Biermann, A. Georges, A. I. Lichtenstein, A. N. Rubtsov, T. Saha-Dasgupta, and O. K. Andersen, *Phys. Rev. B* **76**, 085127 (2007).
- <sup>10</sup>F. Rodolakis, P. Hansmann, J.-P. Rueff, A. Toschi, M. W. Haverkort, G. Sangiovanni, A. Tanaka, T. Saha-Dasgupta, O. K. Andersen, K. Held, M. Sikora, I. Alliot, J.-P. Itié, F. Baudelet, P. Wzietek, P. Metcalf, and M. Marsi, *Phys. Rev. Lett.* **104**, 047401 (2010).
- <sup>11</sup>The terminology of high-energy resolution fluorescence detection (HERFD) has been also proposed for naming the method.
- <sup>12</sup>K. Hämäläinen, D. P. Siddons, J. B. Hastings, and L. E. Berman, *Phys. Rev. Lett.* **67**, 2850 (1991).
- <sup>13</sup>J.-P. Rueff and A. Shukla, *Rev. Mod. Phys.* **82**, 847 (2010).
- <sup>14</sup>P. Glatzel and U. Bergmann, *Coord. Chem. Rev.* **249**, 65 (2005).
- <sup>15</sup>F. de Groot, G. Vanko, and P. Glatzel, *J. Phys.: Condens. Matter* **21**, 104207 (2009).
- <sup>16</sup>P. Hansmann (unpublished).
- <sup>17</sup>C. Gougoussis, M. Calandra, A. Seitsonen, C. Brouder, A. Shukla, and F. Mauri, *Phys. Rev. B* **79**, 045118 (2009).
- <sup>18</sup>G. Vanko, F. M. F. de Groot, S. Huotari, R. J. Cava, T. Lorenz, and M. Reuther, e-print [arXiv:0802.2744](https://arxiv.org/abs/0802.2744).
- <sup>19</sup>S. Lupi, L. Baldassarre, B. Mansart, A. Perucchi, A. Barinov, P. Dudin, E. Papalazarou, F. Rodolakis, J.-P. Rueff, J.-P. Itié, S. Ravy, D. Nicoletti, P. Postorino, P. Hansmann, N. Parragh, A. Toschi, T. Saha-Dasgupta, O. K. Andersen, G. Sangiovanni, K. Held, and M. Marsi, *Nat. Commun.* **1**, 105 (2010).
- <sup>20</sup>A. I. Frenkel, D. M. Pease, J. I. Budnick, P. Metcalf, E. A. Stern, P. Shanthakumar, and T. Huang, *Phys. Rev. Lett.* **97**, 195502 (2006).
- <sup>21</sup>D. M. Pease, A. I. Frenkel, V. Krayzman, T. Huang, P. Shanthakumar, J. I. Budnick, P. Metcalf, F. A. Chudnovsky, and E. A. Stern, *Phys. Rev. B* **83**, 085105 (2011).
- <sup>22</sup>L. Baldassarre, A. Perucchi, D. Nicoletti, A. Toschi, G. Sangiovanni, K. Held, M. Capone, M. Ortolani, L. Malavasi, M. Marsi, P. Metcalf, P. Postorino, and S. Lupi, *Phys. Rev. B* **77**, 113107 (2008).
- <sup>23</sup>S.-K. Mo, H.-D. Kim, J. W. Allen, G.-H. Gweon, J. D. Denlinger, J.-H. Park, A. Sekiyama, A. Yamasaki, S. Suga, P. Metcalf, and K. Held, *Phys. Rev. Lett.* **93**, 076404 (2004).
- <sup>24</sup>F. Rodolakis, B. Mansart, E. Papalazarou, S. Gorovikov, P. Vilmercati, L. Petaccia, A. Goldoni, J. P. Rueff, S. Lupi, P. Metcalf, and M. Marsi, *Phys. Rev. Lett.* **102**, 066805 (2009).
- <sup>25</sup>S.-K. Mo, H.-D. Kim, J. D. Denlinger, J. W. Allen, J.-H. Park, A. Sekiyama, A. Yamasaki, S. Suga, Y. Saitoh, T. Muro, and P. Metcalf, *Phys. Rev. B* **74**, 165101 (2006).
- <sup>26</sup>L. Gregoratti, S. Gunther, J. Kovac, M. Marsi, R. J. Phaneuf, and M. Kiskinova, *Phys. Rev. B* **59**, 2018 (1999).
- <sup>27</sup>S. Gunther, A. Kolmakov, J. Kovac, M. Marsi, and M. Kiskinova, *Phys. Rev. B* **56**, 5003 (1997).
- <sup>28</sup>M. Marsi, S. La Rosa, Y. Hwu, F. Gozzo, C. Coluzza, A. Baldereschi, G. Margaritondo, J. McKinley, S. Baroni, and R. Resta, *J. Appl. Phys.* **71**, 2048 (1992).
- <sup>29</sup>M. Marsi, R. Houdre, A. Rudra, M. Ilegems, F. Gozzo, C. Coluzza, and G. Margaritondo, *Phys. Rev. B* **47**, 6455 (1993).
- <sup>30</sup>A. Schaak, S. Gunther, F. Esch, E. Schutz, M. Hinz, M. Marsi, M. Kiskinova, and R. Imbihl, *Phys. Rev. Lett.* **83**, 1882 (1999).
- <sup>31</sup>D. Eich, U. Herber, U. Groh, U. Stahl, C. Heske, M. Marsi, M. Kiskinova, W. Riedl, R. Fink, and E. Umbach, *Thin Solid Films* **361-362**, 258 (2000).
- <sup>32</sup>A. Filippini and A. Di Cicco, *Phys. Rev. B* **52**, 15135 (1995).
- <sup>33</sup>A. Filippini, A. Di Cicco, and C. R. Natoli, *Phys. Rev. B* **52**, 15122 (1995).
- <sup>34</sup>A. Filippini, *J. Phys. B: At., Mol. Opt. Phys.* **33**, 2835 (2000).